PCCP

View Online
Dynamic Article Links

Cite this: *Phys. Chem. Chem. Phys.*, 2011, **13**, 6211–6222

www.rsc.org/pccp

PAPER

Electronic structures and excitonic transitions in nanocrystalline iron-doped tin dioxide diluted magnetic semiconductor films: an optical spectroscopic study

Wenlei Yu,[a] Kai Jiang,[a] Jiada Wu,[b] Jie Gan,[b] Min Zhu,[c] Zhigao Hu*[a] and Junhao Chu[a]

Received 16th August 2010, Accepted 27th January 2011
DOI: 10.1039/c0cp01503b

Nanocrystalline iron-doped tin dioxide ($Sn_{1-x}Fe_xO_2$) films with x from 0 to 0.2 were prepared on c-sapphire substrates by pulsed laser deposition. X-ray diffraction and Raman scattering analysis show that the films are of the rutile structure at low compositions and an impurity phase related to Fe_2O_3 appears until the x is up to 0.2, suggesting the general change of lattice structure due to the Fe ion substitution. The dielectric functions are successfully determined from 0.0248 to 6.5 eV using the Lorentz multi-oscillator and Tauc-Lorentz dispersion models in the low and high photon energy regions, respectively. With increasing Fe composition, the highest-frequency transverse optical phonons E_u shifts towards a lower energy side and can be well described by $(608 - 178x)$ cm^{-1}. From the transmittance spectra, the fundamental absorption edge is found to be decreased with the Fe composition due to the joint contributions from SnO_2 and Fe_2O_3. It can be observed that the doped films exhibit evident excitonic excitation features, which are strongly related to the Fe doping. Among them, the $6A_{1g} \rightarrow 4T_{2g}$ transition contributes to the onset of optical absorption. Moreover, the remarkable intensity reduction and a red-shift trend with the doping composition, except for the pure film, can be testified by the photoluminescence spectra. It can be concluded that the replacement of Sn with the Fe ion could induce the $2p$–$3d$ hybridization and result in the electronic band structure modification of the $Sn_{1-x}Fe_xO_2$ films.

Introduction

Diluted magnetic semiconductors (DMS) have attracted much attention due to the potential application of both charge and spin of electrons.[1,2] Recently, many investigations have been extensively focused on transition metal (TM) doped wide band gap oxide semiconductors such as zinc oxide (ZnO), titanium dioxide (TiO_2), and tin dioxide (SnO_2) owing to room-temperature ferromagnetism (RTFM).[1,3,4] In particular, SnO_2 film with a wide band gap of 3.6 eV at RT is generally used as gas sensors, transparent conducting electrodes, dye-based solar cells, and catalysts, *etc.*[4,5] The first report of high-temperature FM in SnO_2 film was presented by Ogale *et al.*,[6] who described a Curie temperature of about 650 K in Co-doped film with the 5% composition and a large moment of 7.5 μ_B per Co ion. Subsequently, SnO_2 becomes a promising material in the DMS field and is useful for potential applications requiring the combined magnetic and optical functionality. Many groups have reported that the large sp–d exchange interaction between the magnetic ions and the SnO_2 electron bands will lead to a number of unusual properties such as electronic structure changes, magneto-optical, and optoelectronic effects.[7–9] Although the SnO_2 can be doped with any $3d$ TM ions, Fe is of special interest due to its capability of grain growth inhibition within the SnO_2 matrix.[10] It was found that Cr, Mn, Fe, Co, or Ni doped SnO_2 could feature FM at RT, but the Fe doped one has the largest magnetic moment.[7] Moreover, a metallic electronic structure is obtained only in Fe-doped SnO_2 ($Sn_{1-x}Fe_xO_2$).[3] The dopant composition of Fe could provide a strong relation to the distribution of oxygen vacancy (V_o) and the abundant existence of Fe–O–Fe groups further affect the magnetic properties of Fe-doped films.[3] Based on the recent first-principles calculation, there are not only Fe d states but also the oxygen $2p$ states at the Fermi level, showing strong p–d coupling and hopping in $Sn_{1-x}Fe_xO_2$. Meanwhile, the hybridization will bring about

[a] *Key Laboratory of Polar Materials and Devices, Ministry of Education, Department of Electronic Engineering, East China Normal University, Shanghai 200241, People's Republic of China. E-mail: zghu@ee.ecnu.edu.cn; Fax: +86-21-54345119; Tel: +86-21-54345150*
[b] *Key Laboratory for Advanced Photonic Materials and Devices, Ministry of Education, Department of Optical Science and Engineering, Fudan University, Shanghai 200433, People's Republic of China*
[c] *Department of Physics, Shanghai Jiao Tong University, Shanghai 200240, People's Republic of China*

the crystal distortion, which is expected to induce the FM and high spin polarization.[11] These results indicate that the $Sn_{1-x}Fe_xO_2$ system could be one of the suitable host compounds for DMS realization.

On the other hand, a variety of fabrication methods such as sol–gel,[10] molecular beam epitaxy (MBE),[12] reactive magnetron sputtering,[13] chemical vapor deposition (CVD),[4,14] and pulsed laser deposition (PLD)[2,8] have been employed for the preparation of SnO_2 materials. Among them, the PLD technique has the ability to exceed the solubility of magnetic impurity and to permit high quality film grown at low substrate temperature.[8] The physical behaviors of TM doped SnO_2 are sensitive to the grown situation, experimental condition, substrate temperature, and doping level. No doubt, it is important to study TM doped oxide materials with a wide composition region, in which cations are replaced by TM with different degrees of doping. Furthermore, examination of optical constants (*i.e.* dielectric functions) can help us gain the related electronic band structure of materials and explain the corresponding experimental results, which will be critical for developing the novel spinelectronic and optoelectronic devices. Kim *et al.* found the magneto-optical properties and refractive index at the wavelength of only 1550 nm by optical absorption.[8] Ke *et al.* described the dielectric function of the $SnO_2/SrTiO_3$ film in the ultraviolet-near-infrared (UV-NIR) region using ellipsometry measurements.[12] Unfortunately, there are few reports on the optical constants of TM doped SnO_2 films in a wider photon energy region, especially for dielectric function and TM doping effects.

Raman technique can reveal local structural information because the lattice disorder induces spectral change and modification. On the other hand, infrared (IR) spectroscopy is very powerful to study the phonon mode behavior of semiconductor oxide films. Generally, SnO_2 with the rutile structure belongs to the space group D_{4h}^{14}, of which the normal lattice vibration at the Γ point of the Brillouin zone is given as follows on the basis of group theory:[15] $\Gamma = A_{1g}(R) + A_{2g}(F) + A_{2u}(IR) + B_{1g}(R) + B_{2g}(R) + 2B_{1u}(F) + E_g(R) + 3E_u(IR)$. Among these vibrations, E_u and A_{2u} modes are IR active; A_{1g}, B_{1g}, B_{2g} and E_g are Raman-active modes; while A_{2g} and B_{1u} modes are optically inactive. The corresponding frequencies of the optical phonon modes have been theoretically calculated and experimentally measured.[15,16] Nevertheless, the phonon mode assignation is necessary to further study the coupling between the phonon and magnon in DMS system. Moreover, not much work has been done to extract dispersion parameters such as dielectric function, absorption, the phonon mode frequency, and the damping factor. It is essential to know how the lattice parameters are changed as a function of the Fe composition, in order to systematically understand the composition effects on the vibration properties of the $Sn_{1-x}Fe_xO_2$ films.

Besides the dielectric function and lattice vibration, photoluminescence (PL) emission patterns can also be directly correlated to the electronic band structure of materials and it plays an important role in design, optimization, and evaluation of optoelectronic device performance. In particular, PL spectra can provide some physical properties of the band-band and sub-band electronic transitions under the corresponding excitation line, such as defect-induced energy states, which are crucial for the semiconductor band engineering and opto-electronic fields. For SnO_2 materials, there are some reports about the complex emission bands in the range of 318–640 nm.[17,18] It was argued that the origin of PL emission is mainly based on the electron transfer made by lattice defect, surface state, particle size and V_o. Moreover, few reports on the PL spectra from TM doped SnO_2 films have been presented up to now, taking into account that the magnetic element energy levels in the electronic band structure is still an open issue.[3,7] Therefore, it is desirable to carry out a detail study regarding these essential properties of the $Sn_{1-x}Fe_xO_2$ films over a wide range of magnetic doping.

In this article, microstructure, Raman scattering, transmittance, reflectance and PL emission measurements of diluted magnetic $Sn_{1-x}Fe_xO_2$ films on *c*-sapphire substrates have been studied. The dielectric function of the films in the far-infrared-ultraviolet (FIR-UV) photon energy region are extracted by reproducing the experimental spectra with reasonable optical dispersion models. The magnetic composition and temperature effects on the electronic structure, phonon modes, optical band gap (OBG), and the excitonic transition features have been discussed in detail.

Results and discussion

Structural analysis

The XRD patterns of the films with the Fe composition from 0% to 20% have been shown in Fig. 1. As can be seen, there are (110), (101), (200), (211) and (220) diffraction peaks, which reveal that the $Sn_{1-x}Fe_xO_2$ films are polycrystalline with the rutile structure. For the Fe-doped films, the peak (near 38°) is slightly shifted to a higher diffraction angle, as compared to that of a pure SnO_2 film. The change can be ascribed to decreasing lattice spacing due to the presence of smaller Fe^{3+} ions (0.65 Å) in place of Sn^{4+} (0.72 Å).[10,19] Note that the strongest (110) peak becomes much weaker than other

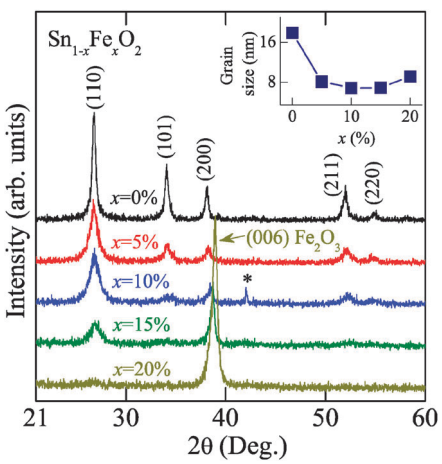

Fig. 1 The XRD patterns of the $Sn_{1-x}Fe_xO_2$ films on *c*-sapphire substrates with different Fe composition. The inset shows that the grain size evaluated from the diffraction peak (110) is varied as the doping composition. The symbol (*) indicates the observed trace from the sapphire substrate.

diffraction peaks for the films doped with $x \geq 15\%$, which is induced by the Fe contributions. The lower and higher Fe compositions could result in different crystalline formations. Moreover, with increasing composition, the broadening of (110) diffraction peak, which is strongly related to film structure, indicates the possible changes in the crystallite size and/or strain. It should be pointed out that the diffraction pattern of the film doped with 20% Fe displays a sharp peak at about 38.9°, which can be assigned to the (006) diffraction peak with good orientation from Fe_2O_3. This demonstrates that the impurity phase appears and Fe ion substitution generally changes the lattice structure. A similar behavior has been reported by Sahana *et al.*[20]

Generally, the XRD technique is frequently applied to estimate the grain size and lattice parameters of films.[9,16] Calculating the *a*-axis lattice constant from the (110) diffraction peak, the average value is about 4.69 Å and it is slightly less than that obtained by others (around 4.76 and 4.73 Å).[10,16] The discrepancy can be ascribed to different crystallinity, preparation method and/or lattice mismatch with the substrate. The grain size can be derived using the well-known Scherrer equation. It was found that the average size is estimated to be about 10 nm for the $Sn_{1-x}Fe_xO_2$ films. A decreasing grain size was observed until the doping is larger than 10% in the inset of Fig. 1, which is possibly related to higher stacking fault density,[10] indicating the doping inhibits particle growth in the lower compositions. Similar phenomena have been also found in ref. 16. Interestingly, there is an obvious increment of the parameter for the film doped with 20% Fe, suggesting that a significant change appears due to different doping mechanism. It indicates that there is the Fe_2O_3 phase, which is further supported by the following Raman analysis. In addition, from the OBG and IR-active lattice vibrations discussed later, the existence of the Fe_2O_3 phase for the highest doping film in the present work is obvious. Therefore, the microstructure and structure evolution are dominated by the Fe_2O_3 phase when the present films are doped with 20% or more Fe.

Raman scattering

In order to give more insight into the structural change of the $Sn_{1-x}Fe_xO_2$ films from the Fe contribution, Raman spectra recorded at RT were presented in Fig. 2. The strong scattering peaks of the films are detected at about 482, 641, and 752 cm^{-1}, corresponding to these fundamental vibration modes (E_g, A_{1g}, and B_{2g}) of the rutile SnO_2, respectively. The phonon modes A_{1g} and B_{2g} are considered as the expansion and contraction of the vibrating mode of Sn–O bonds, while the phonon mode E_g is related to the vibration of oxygen in the oxygen plane.[21] Compared to the pure SnO_2 film, a slight shift in the three peaks is associated with the size effect for the nanocrystalline $Sn_{1-x}Fe_xO_2$.[22] With increasing Fe doping, lower intensity and broadening of the peaks are also found. It reveals that the main characteristics of the tetragonal rutile structure are gradually deteriorated owing to the Fe incorporation, which is consistent with the XRD experiments. In addition, some extra peaks are observed at frequencies of ariound 250–386, 417, 432, 456 and 575 cm^{-1}. It is true that the resonant phenomena could become weaker with the decreasing band gap owing to the Fe introduction, as discussed in the following. Therefore, the Raman scattering intensity can be decreased with increasing Fe composition. Also, the intensity decreases with the Fe composition, suggesting that the Fe substitution might be responsible for the changes in local disorder and defect, such as vacant lattice sites or vacancy cluster.[9] It has been shown that the surface properties are sensitive not only to the grain size but also to the V_o and local disorder, which result in the novel vibration modes of the Raman peak for nanocrystalline SnO_2-base system.[9] Moreover, the shifted and broadened scattering peaks can be varied with the size reduction for the nanocrystalline films, which may be due to the phonon confinement effect.[9,22] It should be noted that the broadening region of 250–386 cm^{-1} can be ascribed to the contributions from intrinsic lattice defects.

From Fig. 2, there are other extra Raman peaks, which are relatively strong and associated with the weak Sn–O bonds. It was reported that such strong scattering bands are related to the symmetric stretching modes and they can be downshifted if some oxygen atoms are not bonded to neighboring Sn atoms, causing the bonds to become weaker.[16] The case of the decreasing intensities of those peaks with the Fe composition reflects the reduction of the Sn–O strength caused by the magnetic doping. Therefore, the varying positions and decreasing intensity for all the peaks can be attributed to the microstructure evolution, which is correlated with the size effect and/or the existence of defects in the $Sn_{1-x}Fe_xO_2$ films. It further confirms that the Fe ion has been successfully incorporated into the SnO_2 lattice and affects the crystal structure, resulting in lattice distortion and the appearance of forbidden Raman phonon modes. At lower doping compositions, the Raman peaks from Fe_2O_3 are weak compared to that of the pure SnO_2 phase. Until the doping composition x reaches 20%, there are some distinct bands located at 249, 292, 407, 608 and 491 cm^{-1}, which agree well with the A_{1g} and E_g phonon modes for hematite Fe_2O_3 (remarked in Fig. 2).[20,23,24] It suggests that the Fe_2O_3 phase plays a dominant role in the Raman spectra at the highest composition in the present work, as seen in the XRD measurements. The spectrum for the film doped with 20% Fe also exhibits a broad band around 660 cm^{-1}, which may be related to the surface states and grain boundary disorder.[23,24] Thus, the variation trend of vibration modes provide valuable evidence of the change in grain size and the influence from the Fe incorporation, which induces more mismatches and defects in the crystalline structure.

Transmittance and reflectance theory

A three-phase layered structure (air/film/substrate) was employed to calculate the UV-NIR transmittance and FIR reflectance spectra of the $Sn_{1-x}Fe_xO_2$ films.[25–27] Fortunately, the effect of the surface rough layer, whose value is much less than the film thickness, can be neglected in the evolution of the optical properties. Because the relatively big light spot (about 4 mm in diameter) and vertical/normal incident accessory (about 10°) are used in the present experiments, the transmittance and reflectance spectra cannot be sensitive to the porous surface layer. Moreover, the porous surface layer contributions

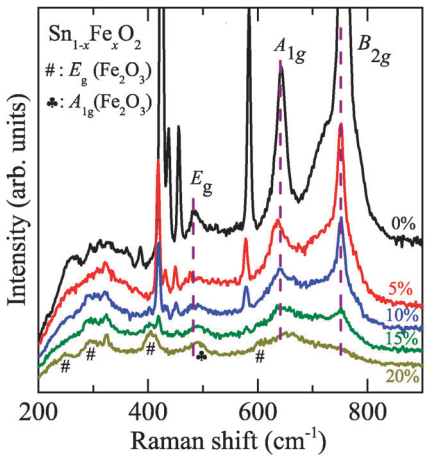

Fig. 2 Raman scattering spectra of the $Sn_{1-x}Fe_xO_2$ films under the excitation line of 325 nm. Note that some peaks from the pure SnO_2 film are cut because of their much stronger intensity. The assignments of the main features for the rutile films and Fe_2O_3 phase are indicated by the dashed lines and symbols, respectively.

should be slight in the IR reflectance spectra due to the smaller values compared with IR wavelength. At near-normal-incident configuration, the following forms describe the transmittance coefficient t and reflectance coefficient r:

$$t = \frac{t_{vf}t_{fs}e^{-i\delta}}{1 + r_{vf}r_{fs}e^{-i2\delta}}, \quad r = \frac{r_{vf} + r_{fs}e^{-i2\delta}}{1 + r_{vf}r_{fs}e^{-i2\delta}} \qquad (1)$$

Here suffix characters v, f, and s correspond to vacuum, film, and substrate, respectively. The phase factor for the film with thickness d has the form $\delta = 2\pi d\sqrt{\varepsilon_f}/\lambda$, where λ is the incident wavelength, and the dielectric function of vacuum is unity. Thus, the transmittance T and reflectance R can be readily obtained from $T = t^*t$, and $R = r^*r$. The multi-reflections from the substrate are not considered here. It should be emphasized that the absorption from the substrate must be taken into account to calculate the transmittance of the film-substrate system.[27]

Generally, the reliability of the fitting method mainly depends on the validity of the dielectric function model. It is a challenge to simulate transmittance spectra of semiconductor film in a wider photon energy region because there is a stronger parameter correlation if a complicated dielectric function model is applied.[27] Fortunately, there are some well-known dispersion functions, which are derived from the band parameters and can be used to express the optical response behavior. Among them, the Tauc-Lorentz (TL) model is obtained from the Tauc joint density of states and the standard quantum mechanical or Lorentz calculation for ε_2 (imaginary part of dielectric function) of a collection of non-interacting atoms.[28] If the multiplied transitions are considered, ε_2 is given by

$$\varepsilon_2(E) = \begin{cases} 0, & E \le E_b \\ \dfrac{AE_0C(E-E_b)^2}{(E^2-E_0^2)^2 + C^2E^2}\dfrac{1}{E}, & E > E_b \end{cases} \qquad (2a)$$

The real part of the dielectric function ε_1 is given by Kramers-Krönig transformation (KKT)

$$\varepsilon_1(E) = \varepsilon_{\infty,\mathrm{UV}} + \frac{2}{\pi}P\int_{E_b}^{\infty}\frac{\xi\varepsilon_2(\xi)}{\xi^2 - E^2}\mathrm{d}\xi. \qquad (2b)$$

Eqn (2) depends on the following five parameters: the parameters A, E_0, C correspond to the amplitude, the peak transition energy, and broadening for the electron transitions, respectively. E_b is the band gap energy and the above four fitting parameters (A, E_0, C and E_b) are in units of energy and $\varepsilon_{\infty,\mathrm{UV}}$ is the high-frequency dielectric constant. The above TL dielectric function model has been successfully applied in many semiconductor and dielectric materials from the transparent to strong absorption region.[12,29] On the other hand, the IR dielectric response function can be typically expressed by the Lorentz multi-oscillator model for the optical phonons. The IR dielectric functions of the $Sn_{1-x}Fe_xO_2$ films can be written as:

$$\tilde{\varepsilon}(\omega) = \varepsilon_{\infty,\mathrm{IR}} + \sum_{k=1}^{4}\frac{S_k\omega_{TO,k}^2}{\omega_{TO,k}^2 - \omega^2 - i\omega\Gamma_k} \qquad (3)$$

Here, $\varepsilon_{\infty,\mathrm{IR}}$, S_k, $\omega_{TO,k}$, Γ_k, and ω represent, in order, the high-frequency dielectric constant, the phonon strength, the phonon frequency, the damping parameter of the transverse optical (TO) phonon, and the frequency of the incident light, respectively.[25] The free carrier effects are neglected because the $Sn_{1-x}Fe_xO_2$ films are nominally undoped. Note that it is nearly impossible that the TL or Lorentz model can explain the complicated optical response behavior of semiconductors and insulators in the wider photon energy region. Therefore, different dielectric function models corresponding to the interband and intraband electronic transition mechanism are necessary to completely describe the contributions from the band structure.[27]

IR-active lattice vibrations

IR reflectance can give information not only about the position of the ions but also their vibration modes in semiconductor crystals. As compared with Raman spectroscopy, IR reflectance technique is based on potentially different selection rules and the incident light can penetrate the films to the substrates, which can present the total effects of film materials studied. Fig. 3 displays the IR reflectance from the $Sn_{1-x}Fe_xO_2$ films in the frequency range of 200–2000 cm^{-1} (0.0248–0.248 eV). The dashed lines are the experimental data and the solid lines are the fitting results with the Lorentz multi-oscillator model. A good agreement can be found in the entire measured frequency region. The best fit parameter values of the Lorentz multi-oscillator model are listed in Table 1. As can be seen, all spectral lineshapes are not strikingly changed corresponding to different Fe composition. However, the distinct variation can be observed in the frequency region of 555–625 cm^{-1}, as shown in the inset of Fig. 3. As compared to the highly reflecting sapphire substrate,[30] the two peaks located at about 247 and 289 cm^{-1} can be assigned to the low-frequency E_u(TO) phonon modes. The phonon frequencies for all films are nearly the same and present a weak composition dependence. For pure SnO_2 film, the sharp dip located at about 605 cm^{-1}, which is correlated to the antisymmetric Sn–O–Sn stretching,[31] is also characterized by the E_u(TO) phonon mode. A small band emerging at around 480 cm^{-1} is identified from the A_{2u}(TO) phonon mode. Owing to the lattice distortions, the highest phonon frequency E_u related to

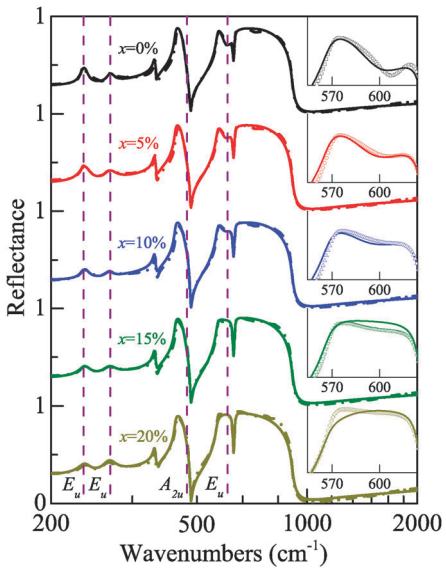

Fig. 3 Experimental infrared reflectance spectra (dotted lines) and the best-fit results (solid lines) of the $Sn_{1-x}Fe_xO_2$ films with different Fe composition. Each spectrum is successively shifted by 1.0 in the vertical direction. For clarity, an enlarged frequency region of 555–625 cm^{-1} from the reflectance spectra are plotted in the insets. The horizontal coordinates are the logarithmic units and the dash lines clearly indicate the phonon modes.

the vertical displacements of Sn and O ions is overlapped with the A_{2u} phonon mode, which is ascribed to the parallel relative displacements.[32] These results suggest that $3E_u$(TO) and A_{2u}(TO) phonon frequencies of polycrystalline $Sn_{1-x}Fe_xO_2$ films are close to those found in single crystal SnO_2.[15] Nevertheless, the doping composition slightly affects the phonon frequency, intensity and broadening. Due to the near-normal incidence ($\sim 10^\circ$), the broadening band at 660–780 cm^{-1} in the reststrahlen band of the sapphire is regarded as the E_u longitudinal optical (LO) polar mode. Similar results can be also observed in polycrystalline SnO_2.[32] The reflectance spectra below 200 cm^{-1} are overlapped with each other for all films and sapphire substrate (not shown), indicating further that the contributions from the free carriers can be neglected.

It should be emphasized that the highest frequency E_u(TO) phonon mode for all films shifts toward the lower energy side with increasing Fe composition (inset of Fig. 8). A linear dependence on the magnetic composition can be well described by $(608 - 178x)$ cm^{-1}, suggesting that the Fe doping into the lattice is responsible for the fluctuations of the E_u(TO) phonon mode. Moreover, the frequency shifts away from its value of pure SnO_2 and slowly approaches the side of the E_u(TO) band near 524 cm^{-1} for well-crystallized hematite Fe_2O_3, which is derived from the main stretches of the Fe–O bonds.[33] It indicates that the crystalline structure of the $Sn_{1-x}Fe_xO_2$ films can transform to that of hematite Fe_2O_3 material with increasing Fe composition, especially for $x = 20\%$ in the present work. It was reported that two modes in the regions of 615–630 cm^{-1} and 570–580 cm^{-1} from the absorption spectra are considered as the IR-active Sn–O stretching volume modes, whose frequencies shift down with the Fe doping, while the grain size linearly decreases as the Fe composition increases from 0 to 1.0.[16] Therefore, it is reasonable that the variation of the highest frequency E_u(TO) phonon mode is induced by the local disorder with replacement of Sn atom by Fe atom and the linear dependence could be strongly related to the difference of the grain size in the $Sn_{1-x}Fe_xO_2$ films.

Furthermore, the increasing trend of the broadening value Γ_3 for the highest frequency E_u(TO) phonon has been found, except for $x = 20\%$, as seen in Table 1. It can be believed that the micro-structure transition of the films indeed appears, which was confirmed by the XRD experiments. It suggests that the crystalline quality significantly changes with the composition, as seen in the XRD and Raman analysis. This is because the Fe effects could result in reductions of the bonding forces for the material and the translational symmetry of the crystal lattice, then lead to a broadening of the E_u(TO) phonon mode.[34,35] Nevertheless, taking into account the size effects observed from the XRD studies and assuming Fe–O bond as the main role, it is possible that the decrease of the mentioned damping could be associated with the abrupt increase in the grain size for the highest doping composition in present work. Similarly, the $\varepsilon_{\infty,IR}$ for the $Sn_{1-x}Fe_xO_2$ films shows an increasing trend from 4.4 to 5.64 with different Fe composition. These values are much higher than the reported ones ($\varepsilon_{\infty\parallel} = 4.17$, $\varepsilon_{\infty\perp} = 3.78$) of single crystal SnO_2,[36] but smaller than those ($\varepsilon_{\infty\parallel} = 6.7$, $\varepsilon_{\infty\perp} = 7$) of Fe_2O_3 obtained from IR spectra.[33] The discrepancy is a distinct sign of the influence from the Fe incorporation on the SnO_2 host matrix and overcompensated action by the Fe_2O_3 phase. It indicates that the Fe introduction could increase the contributions from the high energy side, which results in an enhancement of $\varepsilon_{\infty,IR}$.

Electronic structures and excitonic features

The experimental optical transmittance of the $Sn_{1-x}Fe_xO_2$ films at RT were shown in Fig. 4 with the dotted lines. As compared to pure SnO_2, the decreasing interference oscillation periods demonstrate a smaller thickness value for the doped

Table 1 The Lorentz multi-oscillator parameter values for the $Sn_{1-x}Fe_xO_2$ films are extracted from the best fit of the far-infrared reflectance spectra in Fig. 3

			E_u			E_u			E_u			A_{2u}		
Samples	x (%)	$\varepsilon_{\infty,IR}$	S_1	$\omega_{TO,1}$ (cm^{-1})	Γ_1 (cm^{-1})	S_2	$\omega_{TO,2}$ (cm^{-1})	Γ_2 (cm^{-1})	S_3	$\omega_{TO,3}$ (cm^{-1})	Γ_3 (cm^{-1})	S_4	$\omega_{TO,4}$ (cm^{-1})	Γ_4 (cm^{-1})
A	0	4.40	2.18	246	10.5	0.99	290	15.0	1.04	605	50.2	1.29	477	47.8
B	5	4.80	3.22	247	16.0	1.76	289	23.3	1.10	600	52.3	1.38	473	49.1
C	10	4.89	1.78	248	13.9	0.71	288	13.9	1.12	594	59.9	1.29	469	55.4
D	15	5.18	2.63	248	19.3	2.05	289	25.4	0.60	583	88.9	1.20	473	44.1
E	20	5.64	2.62	247	19.8	2.92	288	23.5	0.37	569	22.0	1.19	474	49.2

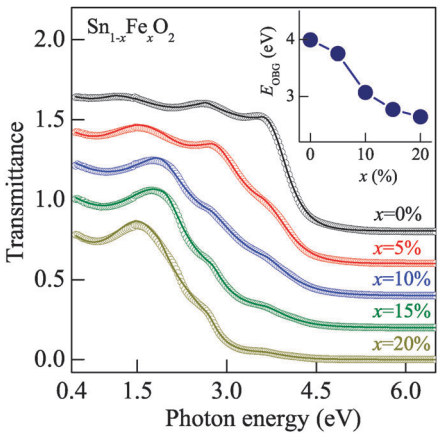

Fig. 4 Experimental transmittance spectra (dotted lines) and the best-fit results (solid lines) of the $Sn_{1-x}Fe_xO_2$ films from the near-infrared to ultraviolet photon energy region. Note that each spectrum is successively shifted by 0.2 in the vertical direction for clarity. The inset shows the composition dependence of the optical band gap in the films.

films. With increasing Fe composition, the absorption edges of the doped films are shifted to the longer wavelengths and reveal a remarkable dependence on the Fe composition. Note that the doped films exhibit some small shoulder structures near the photon energy region of 2–4 eV since the 3*d* electrons form an impurity band in the band gap from the crystal field transition. It again confirms that there is the presence of Fe ions in the SnO_2 lattice. Such shoulder characteristics are also observed in TM doped ZnO and TiO_2 materials.[37,38] Based on the simulation, the parameter values of the TL dielectric function model are summarized in Table 2, and the reproduced transmittance are also plotted in Fig. 4 by the solid lines. Again, a good agreement between the calculated and experimental spectra is obtained in the entire photon energy region, especially near the fundamental absorption edge. It indicates that the TL dispersion function is suitable to express the optical response of the $Sn_{1-x}Fe_xO_2$ films from 0.47 to 6.5 eV. Moreover, the OBG for the $Sn_{1-x}Fe_xO_2$ films can be calculated by considering a direct transition between the valence band (VB) and conduction band (CB).[2,20] In this case, the variation in absorption coefficient (α) as a function of photon energy can be typically fitted to a power law relationship of Tauc: $(\alpha E)^2 \propto (E - E_{OBG})$. So the straight line between $(\alpha E)^2$ and E will provide the OBG value, as seen in Fig. 5(a) for all films. It is clearly found that the OBG decreases rapidly from 3.99 to 2.64 eV with increasing Fe composition, as shown in the inset of Fig. 4. Thus, the behavior of tunable OBG caused by the Fe doping can increase the visible light absorption. The OBG energy of Fe_2O_3 is known to be about 2 eV, which is much smaller than that of SnO_2. The decreasing OBG can be understood in terms of the joint contributions from SnO_2 and Fe_2O_3. Similar phenomena have been reported by Sahana *et al.*[20] Nevertheless, in the nearly identical doping level, the deviation is larger than the results (from 3.89 to 3.11 eV) from transmittance spectra owing to different growth technique and crystalline structures.[20]

The absorption edge of SnO_2 has been assigned to interband transitions from the VB edge with O 2*p* orbitals to the CB edge with Sn 5*s* orbitals.[39,40] In Fe doped rutile SnO_2, O ions around Fe ions form an octahedral crystal field, splitting 3*d* orbitals into lower t_{2g} states and upper e_g states.[3] The three 3*d* (t_{2g}) states are occupied and the other three t_{2g} and four e_g states are empty and located inside the band gap formed by Sn 5*s*- and O 2*p*-like bands.[13] Moreover, the filled Fe 3*d* states are strongly hybridised with the O 2*p* states, giving a broadening band with a width comparable to O 2*p* states.[3] Therefore, increasing Fe content can affect the O 2*p* and Fe 3*d* orbital distributions, which will induce the t_{2g} and e_g states located at different levels in the energy space. This can further result in the band gap decreasing in the $Sn_{1-x}Fe_xO_2$ films. In addition, the intraband and interband electronic transitions are related to the ability of electrons located in bands below the Fermi level to be excited to unoccupied levels above it, and their intensity is proportional to the density of states (DOS).[41] From the first principle calculations, the DOS at the Fermi level is mainly derived from the O 2*p* states and only less than half of the total states were contributed by Fe 3*d* states for $Fe_{0.125}Sn_{0.875}O_2$.[11] Thus, the Fe introduction can affect the electronic band structure of the SnO_2 matrix and result in different spectral response behaviors with the doping composition.

It is pointed out that the pure film does not contain the Fe influence and the excitonic features are only considered in the doped materials. From Table 2, the increase of the Fe composition results in a linear increase in both E_{01} and E_{02}, which can be well expressed by $(1.89 + 1.4x)$ and $(1.82 + 4.4x)$ eV, respectively. The values are less than the corresponding OBG energy for the doped films, indicating the existence of sub-band gap states, as discussed previously. Additionally, the fact that a higher Fe composition corresponding to larger amplitudes (A_1, A_2) of both E_{01} and E_{02} shows a stronger intensity of excitonic transitions. In contrast, the parameter E_{03} presents a linearly decreasing trend with the Fe composition and can be described by

Table 2 The Tauc-Lorentz's parameter values for the $Sn_{1-x}Fe_xO_2$ films are determined from the simulation of ultraviolet-near-infrared transmittance spectra in Fig. 4

				TL_1				TL_2				TL_3			
Samples	x (%)	Thickness (nm)	$\varepsilon_{\infty,UV}$	A_1 (eV)	E_{01} (eV)	C_1 (eV)	E_{b1} (eV)	A_2 (eV)	E_{02} (eV)	C_2 (eV)	E_{b2} (eV)	A_3 (eV)	E_{03} (eV)	C_3 (eV)	E_{b3} (eV)
A	0	232	2.73	4.38	0.55	0.78	1.07	6.5	2.53	0.40	2.62	63.7	4.30	2.75	3.57
B	5	204	2.34	4.33	1.91	2.70	1.87	41.8	1.96	2.77	2.73	112	4.58	5.92	3.55
C	10	152	2.26	11.3	2.07	2.35	1.78	59.4	2.34	1.74	2.70	172	3.61	5.10	3.61
D	15	163	2.32	32.5	2.18	3.08	1.94	53.1	2.56	0.68	2.72	227	3.0	4.24	3.59
E	20	186	2.42	34.9	2.11	2.39	1.84	66.1	2.62	0.90	2.65	226	2.99	4.23	3.53

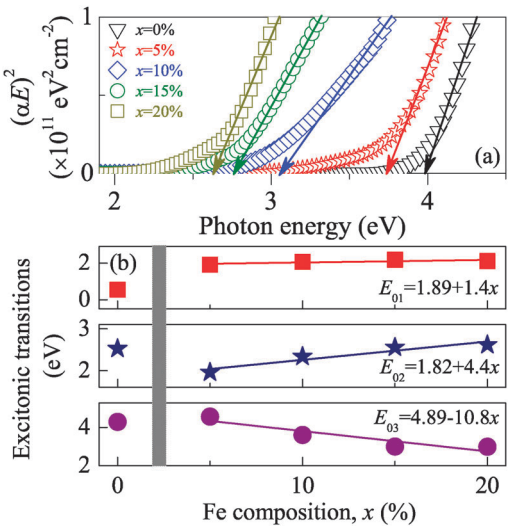

Fig. 5 (a) Tauc plots of the $Sn_{1-x}Fe_xO_2$ films with different Fe composition are applied to determine the band gap by the arrows. (b) The composition dependence of three excitonic transition energies except for the pure SnO_2 film. The solid lines represent the linear fitting results to guide the eyes.

$(4.89 - 10.8x)$ eV. The relations between the three E_0 and Fe composition are plotted in Fig. 5(b). It has been reported that optical transition is expected to occur from Fe t_{2g} to the CB because t_{2g} level is close to the VB in Fe doped TiO_2 materials,[38] which also appear in the $Sn_{1-x}Fe_xO_2$ films. In Fe doped ZnO samples, however, the absorption bands at 450 and 512 nm have been attributed to the Fe ion in tetrahedral co-ordination.[37] Furthermore, we can identify the observed excitations by comparison with similar conditions in Fe_2O_3 and $BiFeO_3$.[24,29,42,43] Dipole-allowed excitations appear above 2.2 eV as O p to Fe d charge transfer in the minority channel. The feature at high energy is related to a strongly hybridized majority channel O p + Fe d → Bi p state excitation.[29,43] Based on the arguments, it can be concluded that E_{01} and E_{02} are related to a collective excitation in hybridization states and charge transfer from Fe $3d$ to CB, respectively. Moreover, the E_{01} energy, which contributes to the onset of optical absorption[29] and has the smallest amplitude (A_1), is close to that of Fe_2O_3 and $BiFeO_3$.[42,43] It could be assigned as $6A_{1g} \rightarrow 4T_{2g}$ excitation, which is on-site Fe ion crystal field transition.[43] Similarly, the high energy E_{03} is assigned to majority channel charge transfer excitation from strongly hybridized O p and Fe d states to Sn p state. Therefore, the effects from the Fe introduction play an important role in the electronic band structure modification, which further affect the optical behaviors of the $Sn_{1-x}Fe_xO_2$ films.

Temperature effects on electronic transitions

Considering that the $Sn_{1-x}Fe_xO_2$ films were prepared by the PLD under the same condition, the trend of optical properties with the temperature could be similar for films with different doping compositions. The film doped with 20% Fe was chosen for the temperature dependence studies due to the most remarkable excitonic features, which are strongly related to the iron doping. The absorbance spectra of the films doped with 20% Fe recorded at 5.3 K, 150 K, and RT are displayed in Fig. 6. As can be seen, the temperature effect on the absorbance is weak due to the presence of the impurity states and the largest shift value from 5.3 K to RT is about 55 meV in the vicinity of E_{01}. Nevertheless, the broadening shoulder structures become stronger with decreasing temperature. The insets present the enlarged energy regions for the three electronic transitions with temperature. It can be clearly observed that the absorbance of E_{01} and E_{02} shift towards a lower value side with decreasing temperature. However, temperature-induced deviation of absorbance for the E_{03} transition presents an opposite trend. The phenomena have been also found in the energies of the three transitions with the composition. It can be ascribed to the electronic band structure variations of the films with temperature. It is worth noting that the shift in the high temperature region (150 K–RT) is larger than that in the low temperature region (5.3–150 K) for all three electronic transitions. On the other hand, two physical mechanisms are generally responsible for the temperature dependence of the excitonic transitions in semiconductor materials: the electron–phonon interaction and the thermal expansion of the lattice. However, the thermal expansion contribution should be slight due to the small ratio of about 2%–20%.[27] The feature with the temperature could be similar to that in other literatures, and it could be correlated mostly to the contribution of electron–phonon interaction.[44–46] Moreover, the total shift of absorbance for the E_{01} is larger than others, which suggests that there is a more remarkable change in hybridization states with different temperature.

As we know, oscillator strength is used as a judgement of the relative strength of the electronic transitions within atomic and molecular systems. The oscillator strength f can be calculated using the partial sum rule: $f = 2c/(N_e\hbar\pi\omega_p^2)\int_{E_1}^{E_2} n\alpha dE$. Here, c is the speed of light, $N_e = 5$ is the number of electrons per Fe site, n is refractive index, α is absorption coefficient, ω_p is the plasma frequency $[\omega_p^2 = e^2\rho/(m\varepsilon_0)]$, e and m are the charge and mass of an electron, ε_0 is vacuum dielectric constant, ρ is the density of Fe sites, and E_1 and E_2 are the photon energies of integration.[43] Fig. 7 describes the values of f for the electronic transitions in the film doped with 20% Fe from 5.3 K to RT. The f values with the magnitude of 10^{-4} are reasonable, compared with some Fe doped oxides.[43,47] With increasing the temperature, the larger values for f_{01} and f_{02} are found, indicating a stronger phonon-magnon interaction,[42] but f_{03} is decreased with increasing temperature. As compared to other magnetic element doped SnO_2 films,[48] the excitonic transitions related to the magnetic ion are readily observed in the low-temperature transmittance spectra for the present $Sn_{1-x}Fe_xO_2$ films. It indicates that the Fe doping can enhance the collective excitations of the SnO_2 system, which provides similar phenomena to other ion-based oxides.[42,43] The temperature dependence behavior can be explained by the fact that spin–orbit coupling relaxes the spin selection rule and the distortion breaks the parity selection rule, which involved odd-parity phonons, then further affects the changes of oscillator strengths.[43,47] Therefore, the Fe incorporation can mainly contribute to the RTFM properties of the $Sn_{1-x}Fe_xO_2$ films because the oscillator strength below the OBG energy

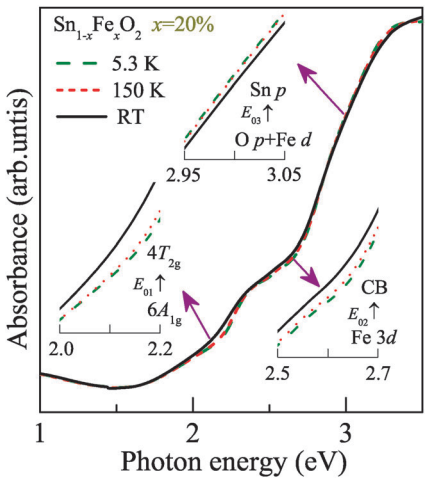

Fig. 6 The absorbance spectra of the $Sn_{1-x}Fe_xO_2$ film doped with 20% Fe were recorded at the temperatures of 5.3 K, 150 K, and RT, respectively. The insets show the enlarged photon energy regions for the excitonic transitions and their physical origin from the band structure.

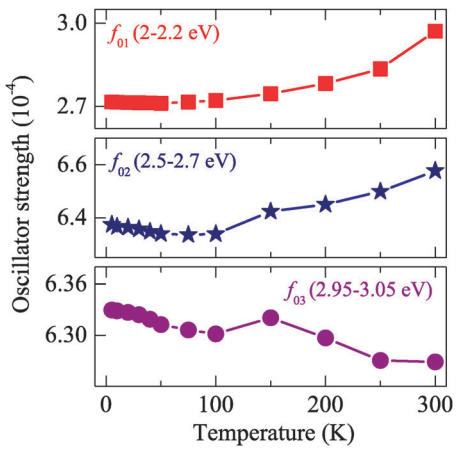

Fig. 7 The oscillator strengths of three excitonic transitions as a function of temperature from 5.3 K to RT for the film doped with 20% Fe. The respective integration regions are given in parentheses.

increases with the temperature, which results in the modification effects on the electronic band structure and free carrier distributions.

Dielectric functions

The dielectric functions of the $Sn_{1-x}Fe_xO_2$ films can be uniquely determined by fitting the model function to the experimental data. It should be emphasized that it is nearly impossible that the TL or Lorentz multi-oscillator model can solely explain the complicated optical response behavior of semiconductors and insulators in the wider photon energy region. Therefore, different dielectric function models corresponding to the interband and intraband electronic transitions are necessary to reasonably describe the contributions from the band structure. The selections of the TL and Lorentz fitting models for different photon energy regiosn could be acceptable to express the optical properties of the present $Sn_{1-x}Fe_xO_2$ films. The real part [Real (ε)] and the imaginary part [Imag (ε)] of dielectric functions from the Lorentz multi-oscillator and TL dispersion models in the different photon energy region for the $Sn_{1-x}Fe_xO_2$ films are shown in Fig. 8 and 9, respectively. In Fig. 8, where the dispersion contribution is mainly derived from IR optical phonon modes, the spectral shapes are found to be similar for all films except for the high frequency side. The various intensities of all peaks indicate that the Fe incorporation might be responsible for the crystalline formation and local disorder. As discussed previously, introduction of Fe results in the lattice distortion and reduction in lattice space symmetry. It is well known that the peak position of Imag (ε) corresponds to the TO phonon mode in IR lattice vibration region. At lower composition, the intensity of E_u(TO) at about 247 cm^{-1} is the strongest and much larger than that of the second peak at about 289 cm^{-1}. However, the situation is opposite when x reaches 20%, and the former is less than the latter. The results can reflect the structure change of the films, which is confirmed by the XRD experiments. From this viewpoint, it can also be found that the effects from the Fe doping are significant for the properties of the above E_u(TO) phonon modes. Moreover, the Imag (ε) is very small at 0.0248 eV, suggesting that it is reasonable to ignore the contributions from the free carries. However, the Imag (ε) is nearly down to zero above 0.08 eV, which shows that the films are transparent in the region.

On the other hand, in the transparent region from Fig. 9, the Real (ε) increases from 3.44 to 4.76 with the Fe composition at the limited energy of 0.47 eV, indicating that the refractive index varies approximately from 1.85 to 2.18. These values are close to those of Mn doped SnO_2 films[48] and the refractive index of the pure film is slightly less than that (about 2.06 at 2 eV) of the $SnO_2/SrTiO_3$ films prepared by MBE.[12] The results may be ascribed to the crystallinity and film packing density of the films. It should be emphasized that there are no obvious dispersion variations in the discontinued energy region of 0.248–0.47 eV due to the transparency of the $Sn_{1-x}Fe_xO_2$ films. Some deviations of Real (ε) at the limited photon energies (0.248 and 0.47 eV) can be found for all films.

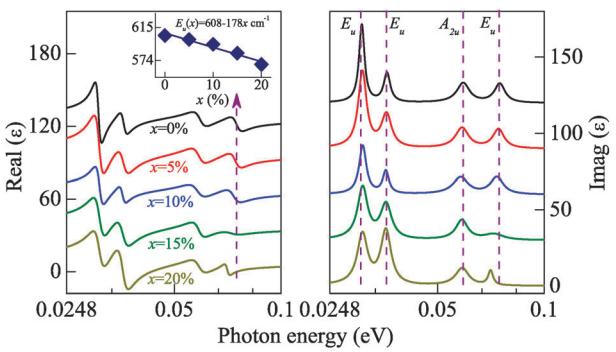

Fig. 8 Evolution of the dielectric functions for the $Sn_{1-x}Fe_xO_2$ films with different composition in the photon energy region of 0.0248–0.1 eV. Note that both Real (ε) and Imag (ε) are vertically shifted by adding 30. To clarify, the horizontal coordinates are the logarithmic units and the dash lines are applied to guide the eyes. The inset shows that the highest frequency E_u(TO) phonon mode linearly decreases with the Fe composition.

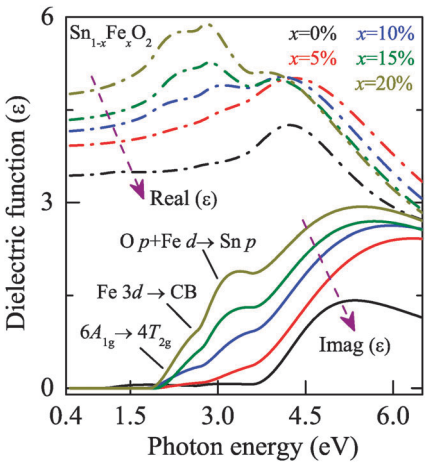

Fig. 9 The Fe composition effects on the dielectric functions of the $Sn_{1-x}Fe_xO_2$ films with different compositions in the photon energy region from 0.47 to 6.5 eV. The arrows indicate a decreasing Fe composition trend and the related excitonic transition features are assigned.

It should be emphasized that the fitting quality for the IR reflectance and UV transmittance spectra is good and the model calculations give a standard deviation of $<10^{-4}$–10^{-5} between the measured and calculated data for all spectra. Moreover, the derived optical constants for the present $Sn_{1-x}Fe_xO_2$ films abide by the general dispersion relation, which is similar to most of the semiconductor and insulator materials. Thus, it can be believed that the optical constants by fitting the spectra could have a similar trend even if other dielectric function models except for different parameter values are applied. Note that the experimental transmittance and reflectance spectra have been recorded in different optical configuration, respectively. Because the background spectra are taken from air and gold/aluminium mirrors, respectively, the absolute transmittance and reflectance may be slightly different. It can induce the fitting deviation between the experimental and theoretical data, which results in the jump phenomena in the transparent region for the $Sn_{1-x}Fe_xO_2$ films. Moreover, the focused light spot on the films could be different for the transmittance and reflectance measurements. It can also result in the slight deviation of the optical constants extracted from the transmittance and reflectance spectra.

The dielectric function increases with the photon energy and the shoulders appear at the range of 2–4 eV for all films, which are more obvious for the films doped with a higher doping composition. It can be attributed to the excitonic effects from the Fe doping. It is worth noting that the Real (ε) decreases with increasing Fe composition except for pure film beyond the photon energy of about 4 eV, where the transmission is down to zero. The behavior can be related to the interband transition and high-energy critical point transitions. Note that the onset absorption from the Imag (ε) is about 2 eV expect for the pure film. The value is close to the Fe crystal field exciton transition E_{01} energy, which agrees well with the above analysis. It can be explained by the previously mentioned hybridization in the $Sn_{1-x}Fe_xO_2$ films. Interestingly, the $\varepsilon_{\infty,IR}$ values are larger than ones ($\varepsilon_{\infty,UV}$) of the TL model in the UV-NIR region for the $Sn_{1-x}Fe_xO_2$ films. The discrepancy may be due to the different fitting range and $\varepsilon_{\infty,IR}$ contains information or influences from that of UV electronic transition. It indicates that the contributions from the high energy electronic transition for the films in the IR region are remarkable compared with that in the UV-NIR region. Note that the parameter ε_∞ accounts for the so-called high frequency limit. Therefore, the dielectric function model should be extrapolated to shorter wavelengths than those studied here. However, the present transmittance spectra cannot detect the performance from high energy side due to a strong absorption and the experimental limitation. Moreover, it is nearly impossible that eqn (2) and (3) can solely explain the complicated behavior of many high energy transitions beyond the band gap energy in semiconductor and dielectric materials. Nevertheless, the values of ε_∞ are well located in a reasonable magnitude region, as compared with some typical wide band gap semiconductors and insulators.[33,49]

Photoluminescence properties

PL spectra are very useful for determining the structures, defects and impurities in nanostructures. The left panel of Fig. 10 presents PL emission spectra from the $Sn_{1-x}Fe_xO_2$ films with excitation at 325 nm. The high energy band emissions, such as 318 nm (3.9 eV) and 350 nm (3.5 eV), are not observed by the present measurement due to the detection limitation and/or the dipole-forbidden nature of first transition for SnO_2.[17,18] In this work, all spectra are characterized by a broadening feature around 2.2 eV, with a small emission shoulder at 1.9 eV, which can be analyzed by Gaussian curve fitting and comparable with the reported ones.[4,50] The positions of both peaks are very close to those in SnO_2 nanostructures and the broadening emission is likely related to the V_o and the shoulder may be originated from Sn interstitials (Sn_i).[4] However, Zhou *et al.* suggested that the observed peak at 2.1 eV is derived from the unoccupied electron states in the dangling bonds at the surface of SnO_2

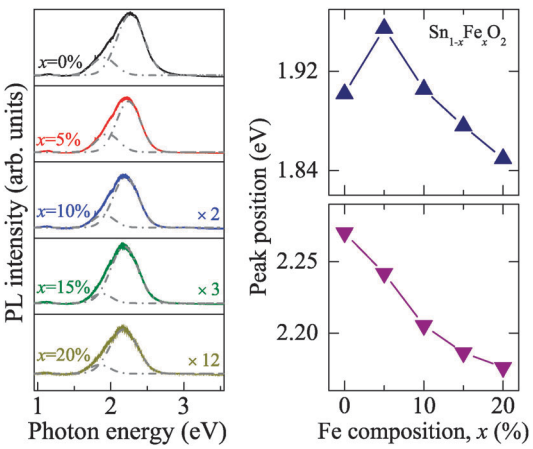

Fig. 10 Photoluminescence spectra of the $Sn_{1-x}Fe_xO_2$ films in the photon energy range of 0.9–3.6 eV. The positions of two emission peaks for all films are obtained from the Gaussian fitting. The right panel shows the corresponding trend with the Fe composition for two emission bands.

crystal.[50] Thus, the electronic transition of both peaks could inversely depend on the various defects or surface states, such as V_o and Sn_i. Moreover, the V_o and Sn_i are known to give rise to shallow donor levels near the CB bottom. It has been argued that the electrons in the CB firstly relax nonradiatively to the defect states and then radiatively recombine with the holes in the VB. The transition process can emit a red band at about 590 nm (2.1 eV), which is similar to the case in SnO_2/*p*-Si heterojunction.[51]

It is widely accepted that the V_o is one of the most common defects in oxides and usually acts as recombination centers in luminescence processes.[17] The first principle calculation also shows that the V_o and Sn_i can be easily induced because they have surprisingly low formation energies and strong mutual interactions.[18] Therefore, these defects can appear and act as trapped states within the band gap for nanostructured SnO_2 films. On the other band, the incorporation of Fe in the films is confirmed and its level is located inside the band gap, which is basically derived from Sn 5*s*- and O 2*p*-like bands.[13] As stated before, the 3*d*–2*p* hybridization, which is essential to mediate the exchange interactions between the doped Fe ions,[11] results in the electronic band structure variations of the $Sn_{1-x}Fe_xO_2$ films. Furthermore, the doping of Fe could provide the influence on the V_o distribution due to the partial replacement of Sn with Fe and the Fe filling in the interstitial. When the Sn_i was affected by the Fe doping, the V_o can be correspondingly changed owing to the interaction and further result in the position and intensity variations of the above two PL emission bands. It can be found that PL intensities for the doped films are much lower than that of pure film under the identical excitation condition. The quenching behavior in the emission intensity was also observed in the $Sn_{1-x}Fe_xO_2$ system.[10] The drastic reduction indicates that the emission is suppressed by the Fe doping owing to increasing the nonradiative recombination processes and the improved metal–metal interaction at higher magnetic compositions.[37,38] The surface state could be another cause for the prominent decreasing of the PL intensity when the grain size approaches nanoscale.[52] In addition, the Fe ions could induce the reduction of donor type V_o, with the peak intensity related to the V_o decreasing correspondingly.

The positions of both peaks obviously shift to a low energy side with the doping composition except for pure film, as can be seen in the right panel of Fig. 10. A possible explanation is that the deep level defects are responsible for the changed bands. This is because the trapped states are associated with the V_o and the Fe dopant, which could be expected to trap the electrons in the electron transfer processes and to make the contribution to the luminescence. It indicates that the varying emissions, which can be ascribed to different luminescent centers, are a result of different grain size and/or deep trap due to the hybridization. Therefore, it can be concluded that the Fe introduction in the SnO_2 lattice is responsible for the above luminescence bands, which affects not only the local disorder but also the positions of V_o, Sn_i, and their distributions, then further modifies the optical properties of the $Sn_{1-x}Fe_xO_2$ films with different composition. In order to further clarify the physical behavior, luminescence experiments for the $Sn_{1-x}Fe_xO_2$ films at low temperatures are necessary in future work.

Experimental

Fabrication of the $Sn_{1-x}Fe_xO_2$ films

Nanocrystalline $Sn_{1-x}Fe_xO_2$ films with the nominal thickness of about 200 nm were deposited on *c*-sapphire substrates by the PLD in the present work. The $Sn_{1-x}Fe_xO_2$ targets with a diameter of 3 cm were prepared using a conventional solid-state reaction sintering. During the preparation, Fe_2O_3 powder was mixed with SnO_2 powder (99.99%) in which the Fe mole fraction was varied as 5%, 10%, 15%, and 20%, respectively. Double-side polished *c*-sapphire wafers were used as the substrates. The substrates were rigorously cleaned in pure ethanol with an ultrasonic bath and were rinsed several times with de-ionized water before the deposition. Finally, the wafers were dried in a pure nitrogen stream before the deposition of the films. The $Sn_{1-x}Fe_xO_2$ films were grown at a substrate temperature of about 450 °C and an oxygen pressure of 5 Pa. The growth chamber was first pumped down to a base pressure of 10^{-4} Pa. A Q-switched pulse yttrium aluminium garnet (Nd:YAG) laser with a wavelength of 532 nm and duration of 5 ns, which works at the repetition rate of 10 Hz and an energy of 40 mJ/pulse, was used for the target ablation. The films were grown immediately after the target was preablated. The distance between the target and substrate was kept at 3 cm and the deposition time was set to about 30 min. Then the films were post-annealed at 1000 °C in air atmosphere by a rapid thermal annealing process. A detailed preparation of the films can be found in ref. 53 and 54.

XRD and optical investigations

The crystalline structures of the $Sn_{1-x}Fe_xO_2$ films on *c*-sapphire substrates were analyzed by X-ray diffraction (XRD) using Cu Kα radiation (D/MAX-2550 V, Rigaku Co.). The spectral transmittance experiments were done with a double beam UV-NIR spectrophotometer (PerkinElmer Lambda 950) from 190 to 2650 nm (0.47–6.5 eV) with a spectral resolution of 2 nm. Especially, the film doped with 20% Fe was put into an optical cryostat (Janis SHI-4-1) and the transmittance spectra at different temperatures (from 5.3 K to RT) were measured using the same spectrophotometer. Because the sapphire substrate is not transparent in the FIR region, the near-normal incident ($\sim 10^\circ$) IR reflectance measurements were carried out over the frequency range from 200 to 2000 cm^{-1} (0.0248–0.248 eV) using a Fourier transform infrared spectrometer (Bruker Vertex 80V). The spectral resolution was 2 cm^{-1} in the low frequency and 4 cm^{-1} in the high frequency, respectively. Different beamsplitters, optimized KBr or 6 μm thick Mylar, were used with DTGS detectors for separate IR regions. Gold and aluminium mirrors, whose absolute reflectances were measured, were taken as the references for the spectra in the high and low frequency regions, respectively. PL and Raman spectra were recorded with a Jobin-Yvon LabRAM HR 800 UV spectrometer, with a He–Cd laser as the excitation light, which is operated at the wavelength of 325 nm (3.82 eV). Note that the samples were at RT for all measurements except for the low temperature transmittance and no mathematical smoothing has been performed for the experimental data.

Conclusion

To summarize, the Fe composition effects on the electronic band structures and optical properties of the $Sn_{1-x}Fe_xO_2$ films have been determined from the FIR to UV photon energy region. The XRD and Raman spectra present a consistent result of the structure variation due to the Fe introduction. It is found that the OBG energy shows a decreasing trend with the Fe composition and the assignment of the excitonic features related to the magnetic ion has been discussed. The three E_0 transition energies linearly depend on the Fe doping and their temperature dependence has been studied for the film doped with 20% Fe, which is mainly associated with the electron–phonon interaction. The absorbance and oscillator strengths for two excitonic transitions E_{01} and E_{02} below the fundamental band gap have similar variation trends with temperature. The red-shift trend of the highest E_u(TO) phonon frequency is observed for the $Sn_{1-x}Fe_xO_2$ films. The dielectric functions in the photon energy range of 0.0248–6.5 eV have been extracted by fitting the experimental data with the Lorentz multi-oscillator and Tauc-Lorentz dispersion models. It was found that the dielectric function increases with the photon energy and the shoulder structures related to the magnetic doping appear at the photon energy range of 2–4 eV. Moreover, two PL emission peaks can be strongly affected by the Fe doping due to the 2*p*–3*d* hybridization. The potential origin for intensity reduction and position variation has been discussed in detail. The present results can provide valuable theoretical and experimental support for SnO_2-base opto-electronic and spinelectronic device realizations.

Acknowledgements

One of the authors (Wenlei Yu) is grateful to Xiangui Chen and Wenjuan Zhang for the technical supports. This work was financially supported by Natural Science Foundation of China (Grant Nos. 60906046 and 11074076), Major State Basic Research Development Program of China (Grant Nos. 2007CB924901 and 2011CB922200), Program of New Century Excellent Talents, MOE (Grant No. NCET-08-0192), Projects of Science and Technology Commission of Shanghai Municipality (Grant Nos. 10DJ1400201, 10SG28, 10ZR1409800, and 09ZZ42), and The Program for Professor of Special Appointment (Eastern Scholar) at Shanghai Institutions of Higher Learning.

References

1 Y. Matsumoto, M. Murakami, T. Shono, H. Hasegawa, T. Fukumura, M. Kawasaki, P. Ahmet, T. Chikyow, S. Koshihara and H. Koinuma, *Science*, 2001, **291**, 854–856.
2 S. J. Liu, C. Y. Liu, J. Y. Juang and H. W. Fang, *J. Appl. Phys.*, 2009, **105**, 013928.
3 X. L. Wang, Z. X. Dai and Z. Zeng, *J. Phys.: Condens. Matter*, 2008, **20**, 045214.
4 L. Zhang, S. H. Ge, Y. L. Zuo, B. M. Zhang and L. Xi, *J. Phys. Chem. C*, 2010, **114**, 7541–7547.
5 A. G. Pereira, A. O. Porto, G. G. Silva, G. M. de Lima, H. G. L. Siebald and J. L. Neto, *Phys. Chem. Chem. Phys.*, 2002, **4**, 4528–4532.
6 S. B. Ogale, R. J. Choudhary, J. P. Buban, S. E. Lofland, S. R. Shinde, S. N. Kale, V. N. Kulkarni, J. Higgins, C. Lanci, J. R. Simpson, N. D. Browning, S. Das Sarma, H. D. Drew, R. L. Greene and T. Venkatesan, *Phys. Rev. Lett.*, 2003, **91**, 077205.
7 C. B. Fitzgerald, M. Venkatesan, L. S. Dorneles, R. Gunning, P. Stamenov, J. M. D. Coey, P. A. Stampe, R. J. Kennedy, E. C. Moreira and U. S. Sias, *Phys. Rev. B: Condens. Matter Mater. Phys.*, 2006, **74**, 115307.
8 H. S. Kim, L. Bi, G. F. Dionne and C. A. Ross, *Phys. Rev. B: Condens. Matter Mater. Phys.*, 2008, **77**, 214436.
9 K. Srinivas, M. Vithal, B. Sreedhar, M. M. Raja and P. V. Reddy, *J. Phys. Chem. C*, 2009, **113**, 3543–3552.
10 S. J. Rani, S. C. Roy, N. Karar and M. C. Bhatnagar, *Solid State Commun.*, 2007, **141**, 214–218.
11 S. J. Hu, S. S. Yan, X. X. Yao, Y. X. Chen, G. L. Liu and L. M. Mei, *Phys. Rev. B: Condens. Matter Mater. Phys.*, 2007, **75**, 094412.
12 C. Ke, Z. Yang, W. Zhu, J. S. Pan and S. Karamat, *J. Appl. Phys.*, 2010, **107**, 013515.
13 Y. R. Park and K. J. Kim, *J. Appl. Phys.*, 2003, **94**, 6401–6404.
14 F. Javier Yusta, Michael L. Hitchman and Sarkis H. Shamlian, *J. Mater. Chem.*, 1997, **7**, 1421–1427.
15 R. S. Katiyar, P. Dawson, M. M. Hargreave and G. R. Wilkinson, *J. Phys. C: Solid State Phys.*, 1971, **4**, 2421–2431.
16 X. Mathew, J. P. Enriquez, C. Mejía-García, G. Contreras-Puente, M. A. Cortes-Jacome, J. A. Toledo-Antonio, J. Hays and A. Punnoose, *J. Appl. Phys.*, 2006, **100**, 073907.
17 X. Xiang, X. T. Zu, L. M. Wan, V. Shutthanadan, P. Nachimuthu and Y. Zhang, *J. Phys. D: Appl. Phys.*, 2008, **41**, 225102.
18 W. C. Zhou, R. B. Liu, Q. Wan, Q. L. Zhang, A. L. Pan, L. Guo and B. S. Zou, *J. Phys. Chem. C*, 2009, **113**, 1719–1726.
19 A. Singhal, S. N. Achary, J. Manjanna, O. D. Jayakumar, R. M. Kadam and A. K. Tyagi, *J. Phys. Chem. C*, 2009, **113**, 3600–3606.
20 M. B. Sahana, C. Sudakar, G. Setzler, A. Dixit, J. S. Thakur, G. Lawes, R. Naik, V. M. Naik and P. P. Vaishnava, *Appl. Phys. Lett.*, 2008, **93**, 231909.
21 K. N. Yu, Y. H. Xiong, Y. L. Liu and C. H. Xiong, *Phys. Rev. B: Condens. Matter*, 1997, **55**, 2666–2671.
22 S. Das, S. Kar and S. Chaudhuri, *J. Appl. Phys.*, 2006, **99**, 114303.
23 D. Bersani, P. P. Lottici and A. Montenero, *J. Raman Spectrosc.*, 1999, **30**, 335–360.
24 A. A. Tahir, K. G. Upul Wijayantha, S. Saremi-Yarahmadi, M. Mazhar and V. McKee, *Chem. Mater.*, 2009, **21**, 3763–3772.
25 Z. G. Hu, M. B. M. Rinzan, S. G. Matsik, A. G. U. Perera, G. V. Winckel, A. Stintz and S. Krishna, *J. Appl. Phys.*, 2005, **97**, 093529.
26 J. Zuo and A. Erbe, *Phys. Chem. Chem. Phys.*, 2010, **12**, 11467–11476.
27 A. B. Djurišić, Y. Chan and E. H. Li, *Mater. Sci. Eng., R*, 2002, **38**, 237–293.
28 G. E. Jellison and F. A. Modine, *Appl. Phys. Lett.*, 1996, **69**, 371–373.
29 P. Chen, N. J. Podraza, X. S. Xu, A. Melville, E. Vlahos, V. Gopalan, R. Ramesh, D. G. Schlom and J. L. Musfeldt, *Appl. Phys. Lett.*, 2010, **96**, 131907.
30 Z. G. Hu, A. B. Weerasekara, N. Dietz, A. G. U. Perera, M. Strassburg, M. H. Kane, A. Asghar and I. T. Ferguson, *Phys. Rev. B: Condens. Matter Mater. Phys.*, 2007, **75**, 205320.
31 P. G. Harrison, N. C. Lloyd, W. Daniell, C. Bailey and W. Azelee, *Chem. Mater.*, 1999, **11**, 896–909.
32 H. Zhang, Y. L. Liu, K. Zhu, G. G. Siu, Y. H. Xiong and C. S. Xiong, *J. Phys.: Condens. Matter*, 1998, **10**, 11121–11127.
33 S. Onari, T. Arai and K. Kudo, *Phys. Rev. B: Solid State*, 1977, **16**, 1717–1721.
34 Z. G. Hu, M. Strassburg, A. Weerasekara, N. Dietz, A. G. U. Pereraa, M. H. Kane, A. Asghar and I. T. Ferguson, *Appl. Phys. Lett.*, 2006, **88**, 061914.
35 W. Limmer, M. Glunk, S. Mascheck, A. Koeder, D. Klarer, W. Schoch, K. Thonke, R. Sauer and A. Waag, *Phys. Rev. B: Condens. Matter*, 2002, **66**, 205209.
36 B. L. Yu, L. J. Guo, Z. T. Yang, C. S. Zhu, F. X. Gan, G. L. Zhang, G. Q. Tang, X. C. Wu and W. J. Chen, *Phys. Lett. A*, 1999, **251**, 67–72.
37 S. Singh and M. S. Ramachandra Rao, *Phys. Rev. B: Condens. Matter Mater. Phys.*, 2009, **80**, 045210.

38 K. Nagaveni, M. S. Hegde and G. Madras, *J. Phys. Chem. B*, 2004, **108**, 20204–20212.
39 K. C. Mishra, K. H. Johnson and P. C. Schmidt, *Phys. Rev. B: Condens. Matter*, 1995, **51**, 13972–13976.
40 Ph. Barbarat, S. F. Matar and G. Le Blevennec, *J. Mater. Chem.*, 1997, **7**, 2547–2550.
41 F. Yubero, V. M. Jiménez and A. R. González-Elipe, *Surf. Sci.*, 1998, **400**, 116–126.
42 A. I. Galuza, A. B. Beznosov and V. V. Eremenko, *Low Temp. Phys.*, 1998, **24**, 726–729.
43 X. S. Xu, T. V. Brinzari, S. Lee, Y. H. Chu, L. W. Martin, A. Kumar, S. McGill, R. C. Rai, R. Ramesh, V. Gopalan, S. W. Cheong and S. W. Musfeldt, *Phys. Rev. B: Condens. Matter Mater. Phys.*, 2009, **79**, 134425.
44 W. W. Li, J. J. Zhu, J. D. Wu, J. Sun, M. Zhu, Z. G. Hu and J. H. Chu, *ACS Appl. Mater. Interfaces*, 2010, **2**, 2325–2332.
45 S. A. Lourenco, I. F. L. Dias, J. L. Duarte, E. Laureto, E. A. Meneses, J. R. Leite and I. Mazzaro, *J. Appl. Phys.*, 2001, **89**, 6159–6164.
46 Q. X. Guo, M. Nishio and H. Ogawa, *Phys. Rev. B: Condens. Matter*, 2001, **64**, 113105.
47 G. B. Scott, D. E. Lacklison and J. L. Page, *Phys. Rev. B: Solid State*, 1974, **10**, 971–986.
48 W. L. Yu, W. W. Li, J. D. Wu, J. Sun, J. J. Zhu, M. Zhu, Z. G. Hu and J. H. Chu, *J. Phys. Chem. C*, 2010, **114**, 8593–8600.
49 J. Robertson, K. Xiong and S. J. Clark, *Thin Solid Films*, 2006, **496**, 1–7.
50 J. X. Zhou, M. S. Zhang, J. M. Hong and Z. Yin, *Solid State Commun.*, 2006, **138**, 242–246.
51 Z. Z. Yuan, D. S. Li, M. H. Wang, P. L. Chen, D. R. Gong, P. H. Cheng and D. R. Yang, *Appl. Phys. Lett.*, 2008, **92**, 121908.
52 R. K. Selvan, I. Perelshtein, N. Perkas and A. Gedanken, *J. Phys. Chem. C*, 2008, **112**, 1825–1830.
53 W. W. Li, Z. G. Hu, J. D. Wu, J. Sun, M. Zhu, Z. Q. Zhu and J. H. Chu, *J. Phys. Chem. C*, 2009, **113**, 18347–18352.
54 K. Gao, W. Zhang, J. Sun, N. Xu, Z. F. Ying, Q. Li, J. Gan and J. D. Wu, *J. Phys. Chem. C*, 2009, **113**, 19139–19144.

